

1     **Utsu aftershock productivity law explained from geometric operations on the**  
2                                   **permanent static stress field of mainshocks**

3                                   Arnaud Mignan\*

4

5     Institute of Geophysics, Swiss Federal Institute of Technology, Zurich

6     *Address:* ETHZ, Institute of Geophysics, NO H66, Sonneggstrasse 5, CH-8092 Zurich

7

8     *Correspondence to:* [arnaud.mignan@sed.ethz.ch](mailto:arnaud.mignan@sed.ethz.ch)

9

10 *Abstract:* The aftershock productivity law is an exponential function of the form  
11  $K \propto \exp(\alpha M)$  with  $K$  the number of aftershocks triggered by a given mainshock of  
12 magnitude  $M$  and  $\alpha \approx \ln(10)$  the productivity parameter. This law remains empirical  
13 in nature although it has also been retrieved in static stress simulations. Here, we  
14 parameterize this law using the Solid Seismicity Postulate (SSP), the basis of a  
15 geometrical theory of seismicity where seismicity patterns are described by  
16 mathematical expressions obtained from geometric operations on a permanent static  
17 stress field. We first test the SSP that relates seismicity density to a static stress step  
18 function. We show that it yields a power exponent  $q = 1.96 \pm 0.01$  for the power-law  
19 spatial linear density distribution of aftershocks, once uniform noise is added to the  
20 static stress field, in agreement with observations. We then recover the exponential  
21 function of the productivity law with a break in scaling obtained between small and  
22 large  $M$ , with  $\alpha = 1.5\ln(10)$  and  $\ln(10)$ , respectively, in agreement with results from  
23 previous static stress simulations. Possible biases of aftershock selection, verified to  
24 exist in Epidemic-Type Aftershock Sequence (ETAS) simulations, may explain the  
25 lack of break in scaling observed in seismicity catalogues. The existence of the  
26 theoretical kink remains however to be proven. Finally, we describe how to estimate  
27 the Solid Seismicity parameters (activation density  $\delta_+$ , aftershock solid envelope  $r_*$   
28 and background stress amplitude range  $\Delta\sigma_*$ ) for large  $M$  values.

29

## 30 **1. Introduction**

31 Aftershocks, one of the most studied patterns observed in seismicity, are  
32 characterized by three empirical laws, which are functions of time, such as the  
33 Modified Omori law (e.g., Utsu et al., 1995), space (e.g., Richards-Dinger et al., 2010;  
34 Moradpour et al., 2014), and mainshock magnitude (Utsu, 1970a; b; Ogata, 1988).

35 The present study focuses on the latter relationship, i.e., the Utsu aftershock  
 36 productivity law, which describes the total number of aftershocks  $K$  produced by a  
 37 mainshock of magnitude  $M$  as  
 38  $K(M) = K_0 \exp[\alpha(M - m_0)]$  (1)  
 39 with  $m_0$  the minimum magnitude cutoff (Utsu, 1970b; Ogata, 1988). This relationship  
 40 was originally proposed by Utsu (1970a; b) by combining two other empirical laws,  
 41 the Gutenberg-Richter relationship (Gutenberg and Richter, 1944) and Båth's law  
 42 (Båth, 1964), respectively:

$$43 \begin{cases} N(\geq m) = A \exp[-\beta(m - m_0)] \\ N(\geq M - \Delta m_B) = 1 \end{cases} \quad (2)$$

44 with  $N$  the average number of events above magnitude  $m$ ,  $A$  a seismic activity  
 45 constant,  $\beta$  the magnitude size ratio (or  $b = \beta/\ln(10)$  in base-10 logarithmic scale) and  
 46  $\Delta m_B$  the magnitude difference between the mainshock and its largest aftershock, such  
 47 that

$$48 K(M) = N(\geq m_0 | M) = \exp(-\beta \Delta m_B) \exp[\beta(M - m_0)] \quad (3)$$

49 with  $K_0 = \exp(-\beta \Delta m_B)$  and  $\alpha \equiv \beta$ . Eq. (3) was only implicit in Utsu (1970a) and  
 50 not exploited in Utsu (1970b) where  $K_0$  was fitted independently of the value taken by  
 51 Båth's parameter  $\Delta m_B$ . The  $\alpha$ -value was in turn decoupled from the  $\beta$ -value in later  
 52 studies (e.g., Seif et al. (2017) and references therein).

53 Although it seems obvious that Eq. (1) can be explained geometrically if the  
 54 volume of the aftershock zone is correlated to the mainshock surface area  $S$  with

$$55 S(M) = 10^{M-4} = \exp[\ln(10)(M - 4)] \quad (4)$$

56 (Kanamori and Anderson, 1975; Yamanaka and Shimazaki, 1990; Helmstetter, 2003),  
 57 there is so far no analytical, physical expression of Eq. (1) available. Although Hainzl  
 58 et al. (2010) retrieved the exponential behavior in numerical simulations where

59 aftershocks were produced by the permanent static stress field of mainshocks of  
60 different magnitudes, it remains unclear how  $K_0$  and  $\alpha$  relate to the underlying  
61 physical parameters.

62 The aim of the present article is to describe the Utsu aftershock productivity  
63 equation (Eq. 1) in terms of a geometrical theory of seismicity coined “Solid  
64 Seismicity”, where the Eq. (4) scaling is parameterized using the Solid Seismicity  
65 Postulate (SSP). The SSP has already been shown to effectively explain other  
66 empirical laws of both natural and induced seismicity from simple geometric  
67 operations on a permanent static stress field (Mignan, 2012; 2016a). The theory is  
68 applied here for the first time to describe aftershocks.

69

## 70 **2. Physical Expression of the Aftershock Productivity Law**

### 71 *2.1. Demonstration of the productivity law by geometric operations*

72 “Solid Seismicity”, a geometrical theory of seismicity, is based on the  
73 following Postulate (Mignan et al., 2007; Mignan, 2008, 2012; 2016a):

74

75 **Solid Seismicity Postulate (SSP):** *Seismicity can be strictly categorized*  
76 *into three regimes of constant spatiotemporal densities  $\delta$  – background*  
77  *$\delta_0$ , quiescence  $\delta_-$  and activation  $\delta_+$  (with  $\delta_- \ll \delta_0 \ll \delta_+$ ) - occurring*  
78 *respective to the static stress step function:*

$$79 \quad \delta(\sigma) = \begin{cases} \delta_- & , \sigma < -\Delta\sigma_* \\ \delta_0 & , \sigma \leq |\pm\Delta\sigma_*| \\ \delta_+ & , \sigma > \Delta\sigma_* \end{cases} \quad (5)$$

80 *with  $\sigma$  the static stress [stress unit],  $\Delta\sigma_*$  the background stress amplitude*  
81 *range [stress unit], a stress threshold value separating two seismicity*

82 *regimes, and  $\delta$  the spatial density of events [number of events per unit of*  
83 *volume] per seismicity regime.*

84

85 We mean by “strictly categorized” that any seismicity population is either part of the  
86 background, quiescence or activation regime (or class), with no other regime/class  
87 possible (i.e., a sort of hard labelling). Based on this Postulate, Mignan (2012)  
88 demonstrated the power-law behavior of precursory seismicity in agreement with the  
89 observed time-to-failure equation (Varnes, 1989), while Mignan (2016a)  
90 demonstrated both the observed parabolic spatiotemporal front and the linear  
91 relationship with injection-flow-rate of induced seismicity (Shapiro and Dinske,  
92 2009). It remains unclear whether the SSP has a physical origin or not. If not, it would  
93 still represent a reasonable approximation of the linear relationship between event  
94 production and static stress field in a simple clock-change model (Hainzl et al., 2010;  
95 Fig. 1a). For the testing of the SSP on the observed spatial distribution of aftershocks,  
96 see section 2.2. The power of Eq. (5) is that it allows defining seismicity patterns in  
97 terms of “solids” described by the spatial envelope  $r_* = r(\sigma = \pm\Delta\sigma_*)$  where  $r$  is the  
98 distance from the static stress source (e.g., mainshock rupture) and  $r_*$  the distance  $r$  at  
99 which there is a change of regime (quiescence/background at  $\sigma = -\Delta\sigma_*$  or  
100 background/activation at  $\sigma = \Delta\sigma_*$ ). The spatiotemporal rate of seismicity is then a  
101 mathematical expression defined by the density of events  $\delta$  times the volume  
102 characterized by  $r_*$  (see previous demonstrations in Mignan et al. (2007) and Mignan  
103 (2011; 2012; 2016a) where simple algebraic expressions were obtained).

104 In the case of aftershocks, we define the static stress field of the mainshock by

105 
$$\sigma(r) = -\Delta\sigma_0 \left[ \left( 1 - \frac{c^3}{(r+c)^3} \right)^{-1/2} - 1 \right] \quad (6)$$

106 with  $\Delta\sigma_0 < 0$  the mainshock stress drop,  $c$  the crack radius and  $r$  the distance from the  
107 crack. Eq (6) is a simplified representation of stress change from slip on a planar  
108 surface in a homogeneous elastic medium. It takes into account both the square root  
109 singularity at crack tip and the  $1/r^3$  falloff at higher distances (Dieterich, 1994; Fig.  
110 1b). It should be noted that this radial static stress field does not represent the  
111 geometric complexity of Coulomb stress fields (Fig. 2a). However we are here only  
112 interested in the general behavior of aftershocks with Eq. (6) retaining the first-order  
113 characteristics of this field (i.e., on-fault seismicity; Fig. 2b), which corresponds to the  
114 case where the mainshock relieves most of the regional stresses and aftershocks occur  
115 on optimally oriented faults. It is also in agreement with observations, most  
116 aftershocks being located on and around the mainshock fault traces in Southern  
117 California (Fig. 2c; see section “Observations & Model Fitting”). The occasional  
118 cases where aftershocks occur off-fault (e.g., Ross et al., 2017) can be explained by  
119 the mainshock not relieving all of the regional stress (King et al., 1994; Fig. 2d).

120 For  $r_* = r(\sigma = \Delta\sigma_*)$ , Eq. (6) yields the aftershock solid envelope of the form:

$$121 \quad r_*(c) = \left\{ \frac{1}{\left[1 - \left(1 - \frac{\Delta\sigma_*}{\Delta\sigma_0}\right)^{-2}\right]^{1/3}} - 1 \right\} c = Fc, \quad (7)$$

122 function of the crack radius  $c$  and of the ratio between background stress amplitude  
123 range  $\Delta\sigma_*$  and stress drop  $\Delta\sigma_0$  (Fig. 1c). With  $\Delta\sigma_0$  independent of earthquake size  
124 (Kanamori and Anderson, 1975; Abercrombie and Leary, 1993) and  $\Delta\sigma_*$  assumed  
125 constant,  $r_*$  is directly proportional to  $c$  with proportionality constant, or stress factor,  
126  $F$  (Eq. 7). Geometrical constraints due to the seismogenic layer width  $w_0$  then yield

$$127 \quad c(M) = \begin{cases} \left(\frac{S(M)}{\pi}\right)^{1/2} & , S(M) \leq \pi w_0^2 \\ w_0 & , S(M) > \pi w_0^2 \end{cases} \quad (8)$$

128 with  $S$  the rupture surface area defined by Eq. (4) and  $c$  becoming an effective crack  
 129 radius (Kanamori and Anderson, 1975; Fig. 1d). Note that the factor of 2 (i.e., using  
 130  $w_0$  instead of  $w_0/2$ ) comes from the free surface effect (e.g., Kanamori and Anderson,  
 131 1975; Shaw and Scholz, 2001).

132 The aftershock productivity  $K(M)$  is then the activation density  $\delta_+$  times the  
 133 volume  $V_*(M)$  of the aftershock solid. For the case in which the mainshock relieves  
 134 most of the regional stress, stresses are increased all around the rupture (King et al.,  
 135 1994), which is topologically identical to stresses increasing radially from the rupture  
 136 plane (Fig. 2a-b). It follows that the aftershock solid can be represented by a volume  
 137 of contour  $r_*(M)$  from the rupture plane geometric primitive, i.e., a disk or a  
 138 rectangle, for small and large mainshocks, respectively. This is illustrated in Figure  
 139 3a-b and can be generalized by

$$140 \quad V_*(M) = 2r_*(M)S(M) + \frac{\pi}{2}r_*^2(M)d \quad (9)$$

141 where  $d$  is the distance travelled around the geometric primitive by the geometric  
 142 centroid of the semi-circle of radius  $r_*(M)$  (i.e., Pappus's Centroid Theorem), or

$$143 \quad d = \begin{cases} 2\pi \left( c(M) + \frac{4}{3\pi} r_*(M) \right) & , c(M) + r_*(M) \leq \frac{w_0}{2} \\ 2w_0 & , c(M) + r_*(M) > \frac{w_0}{2} \end{cases} \quad (10)$$

144 For the disk, the volume (Eq. 9) corresponds to the sum of a cylinder of radius  $c(M)$   
 145 and height  $2r_*(M)$  (first term) and of half a torus of major radius  $c(M)$  and minus  
 146 radius  $r_*(M)$  (second term). For the rectangle, the volume is the sum of a cuboid of  
 147 length  $l(M)$  (i.e., rupture length), width  $w_0$  and height  $2r_*(M)$  (first term) and of a  
 148 cylinder of radius  $r_*(M)$  and height  $w_0$  (second term; see red and orange volumes,  
 149 respectively, in Figure 3a-c). Finally inserting Eqs. (7), (8) and (10) into (9), we  
 150 obtain

$$151 \quad K(M) = \delta_+ \begin{cases} \left[ \frac{2F}{\sqrt{\pi}} + F^2 \sqrt{\pi} \left( 1 + \frac{4}{3\pi} F \right) \right] S^{3/2}(M) & , S(M) \leq \left( \frac{w_0 \sqrt{\pi}}{2(1+F)} \right)^2 \\ \frac{2F}{\sqrt{\pi}} S^{3/2}(M) + F^2 w_0 S(M) & \left( \frac{w_0 \sqrt{\pi}}{2(1+F)} \right)^2 < S(M) \leq \pi w_0^2 \\ 2F w_0 S(M) + \pi F^2 w_0^3 & , S(M) > \pi w_0^2 \end{cases}$$

152 (11)

153 which is represented in Figure 3d. Considering the two main regimes only (small  
154 versus large mainshocks) and inserting Eq. (4) into (11), we get

$$155 \quad K(M) = \delta_+ \begin{cases} \left[ \frac{2F}{\sqrt{\pi}} + F^2 \sqrt{\pi} \left( 1 + \frac{4}{3\pi} F \right) \right] \exp \left[ \frac{3 \ln(10)}{2} (M - 4) \right] & , \text{small } M \\ 2F w_0 \exp[\ln(10)(M - 4)] + \pi F^2 w_0^3 & , \text{large } M \end{cases} \quad (12)$$

156 which is a closed-form expression of the same form as the original Utsu productivity  
157 law (Eq. 1). Note that  $K$  and  $\delta_+$  are both, implicitly, function of the selected minimum  
158 aftershock magnitude threshold  $m_0$ .

159 Here, we predict that the  $\alpha$ -value decreases from  $3 \ln(10)/2 \approx 3.45$  to  $\ln(10) \approx$   
160  $2.30$  when switching regime from small to large mainshocks (or from 1.5 to 1 in base-  
161 10 logarithmic scale). It should be noted that Hainzl et al. (2010) observed the same  
162 break in scaling in static stress transfer simulations, which corroborates our analytical  
163 findings. Hainzl et al. (2010) simulated aftershocks using the clock-change model  
164 where events were advanced in time by the static stress change produced by a  
165 mainshock in a three-dimensional medium. They explained the scaling break  
166 observed in simulation as a transition from 3D to 2D scaling regime when the  
167 mainshock rupture dimension approached  $w_0$ , which is compatible with the present  
168 demonstration. For large  $M$ , the scaling is fundamentally the same as in Eq. (4). Since  
169 that relation also explains the slope of the Gutenberg-Richter law (see physical  
170 explanation given by Kanamori and Anderson, 1975), it follows that  $\alpha \equiv \beta$ , which is  
171 also in agreement with the original formulation of Utsu (1970a; b; Eq. 3).

172



173 2.2. Testing of the SSP on the aftershock spatial distribution

174 The SSP predicts a step-like behavior of the aftershock spatial density for an  
175 idealized smooth static stress field (Fig. 4a-b), which is in disagreement with real  
176 aftershock observations. A number of studies have shown that the spatial linear  
177 density distribution of aftershocks  $\rho$  is well represented by a power-law, expressed as  
178 
$$\rho(r) \propto r^{-q} \quad (13)$$
  
179 with  $r$  the distance from the mainshock and  $q$  the power-law exponent. This parameter  
180 ranges over  $1.3 \leq q \leq 2.5$  (Felzer and Brodsky, 2006; Lipiello et al., 2009; Marsan and  
181 Lengliné, 2010; Richards-Dinger et al., 2010; Shearer, 2012; Gu et al., 2013;  
182 Moradpour et al., 2014; van der Elst and Shaw, 2015). Although Felzer and Brodsky  
183 (2004) suggested a dynamic stress origin for aftershocks, their results were later on  
184 questioned by Richards-Dinger et al. (2010). Most of the studies cited above suggest  
185 that the  $q$ -value is explained from a static stress process. As for the examples of  
186 aftershocks shown to be dynamically triggered (e.g., Fan and Shearer, 2016), they are  
187 too few to alter the aftershock productivity law and too remote to be consistently  
188 defined as aftershocks in cluster methods.

189 In a more realistic setting, the static stress field must be heterogeneous (due to  
190 the occurrence of previous events and other potential stress perturbations). We  
191 therefore simulate the static stress field by adding a uniform random component  
192 bounded over  $\pm\Delta\sigma_*$  following Mignan (2011) (see also King and Bowman, 2003).  
193 Note that any deviation above  $\Delta\sigma_*$  would be flattened to  $\Delta\sigma_*$  over time by temporal  
194 diffusion (so-called “historical ghost static stress field” in Mignan, 2016a). Figure 4c  
195 shows the resulting stress field and Figure 4d the predicted aftershock spatial density.  
196 Adding uniform noise blurs the contour of the aftershock solid, switching the  
197 aftershock spatial density from a step function (Fig. 4b) to a power-law (Fig. 4d). We

198 fit Eq. (13) to the simulated data using the Maximum Likelihood Estimation (MLE)  
199 method with  $r_{min} = r_*$  (Clauset et al., 2009) and find  $q = 1.96 \pm 0.01$ , in agreement with  
200 the aftershock literature. This result alone is however insufficient to prove the validity  
201 of the SSP.

202

### 203 **3. Observations & Model Fitting**

#### 204 *3.1. Data*

205 We consider the case of Southern California and extract aftershock sequences  
206 from the relocated earthquake catalog of Hauksson et al. (2012) defined over the  
207 period 1981-2011, using the nearest-neighbor method (Zaliapin et al., 2008; used with  
208 its standard parameters originally calibrated for Southern California, considering only  
209 the first aftershock generation). Only events with magnitudes greater than  $m_0 = 2.0$  are  
210 considered (a conservative estimate following results of Tormann et al. (2014);  
211 saturation effects immediately after the mainshock are negligible when considering  
212 entire aftershock sequences; Helmstetter et al., 2005).

213

#### 214 *3.2. Aftershock spatial density distribution*

215 Figure 5a represents the spatial linear density distribution of aftershocks  $\rho(r)$   
216 for the four largest strike-slip mainshocks in Southern California: 1987  $M=6.6$   
217 Superstition Hills, 1992  $M=7.3$  Landers, 1999  $M=7.1$  Hector Mine, and 2010  $M=7.2$   
218 El Mayor. The distance between mainshock and aftershocks is calculated as  
219  $r = \sqrt{(x - x_0)^2 + (y - y_0)^2}$  with  $(x, y)$  the aftershock coordinates and  $(x_0, y_0)$  the  
220 coordinates of the nearest point to the mainshock fault rupture (as depicted in Figure  
221 2c). The dashed black lines shown in Figure 5a are visual guides to  $q = 1.96$ , showing  
222 that the SSP is compatible with real aftershock observations.

223 Comparing Figure 5a to Figure 4d suggests that  $r_*$  can be roughly estimated  
 224 from the spatial linear density plot, being the maximum distance  $r$  at which the  
 225 plateau ends, here leading to  $r_* \approx 1$  km. This parameter is constant for different large  
 226  $M$  values since both  $w_0$  and  $\Delta\sigma_0$  are constant while  $\Delta\sigma_*$  is also *a priori* a constant. We  
 227 can then estimate the ratio  $\Delta\sigma_*/\Delta\sigma_0$  from Eq. (7). However the result is ambiguous  
 228 due to uncertainties on the width  $w_0$ . For  $w_0 = \{5, 10, 15\}$  km, we get  $\Delta\sigma_*/\Delta\sigma_0 = \{-$   
 229  $0.54, -1.01, -1.38\}$ .

230 As for the plateau value  $\rho(r < r_*)$ , it provides an estimate of the aftershock  
 231 activation density  $\delta_+$  with

$$232 \quad \delta_+ = \frac{\rho(M, r < r_*)}{\exp[\ln(10)(M-4)]} \quad (14)$$

233 a volumetric density, i.e. the linear density  $\rho$  normalized by the mainshock rupture  
 234 area (Eq. 4). Due to the fluctuations in  $\rho(r < r_*)$ ,  $\delta_+$  will be estimated from the  
 235 productivity law instead (see section 3.3) and  $\rho(r < r_*)$  then estimated from Eq. (14)  
 236 (horizontal dashed colored lines), as detailed below.

237 It should be noted that we consider only the first-generation aftershocks to  
 238 avoid  $\rho$  heterogeneities from secondary aftershock clusters occurring off-fault. An  
 239 example of such heterogeneity/anisotropy is illustrated by the Landers-Big Bear case  
 240 (Fig. 2c; dotted colored curve on Fig. 5a). Those cases are not systematic and  
 241 therefore not considered in the aftershock productivity law. However they are also  
 242 due to static stress changes (e.g., King et al., 1994) with the anisotropic effects  
 243 explainable by Solid Seismicity through the concept of “historical ghost static stress  
 244 field” (Mignan, 2016a).

245

246 *3.3. Aftershock productivity law*

247 The observed number  $n$  of aftershocks of magnitude  $m \geq m_0$  produced by a  
 248 mainshock of magnitude  $M$  (for a total of  $N$  mainshocks) in Southern California is  
 249 shown in Figures 5b (for large  $M \geq 6$ ) and 6a (for the full range  $M \geq m_0$ ). We fit Eq.  
 250 (1) to the data using the MLE method with the log-likelihood function

$$251 \quad LL(\theta; X = \{n_i; i = 1, \dots, N\}) = \sum_{i=1}^N [n_i \ln[K_i(\theta)] - K_i(\theta) - \ln(n_i!)] \quad (15)$$

252 for a Poisson process, representing the stochasticity of the count  $K$  of aftershocks  
 253 produced by a mainshock at any given time. Inserting Eq. (1) in Eq. (15) yields

$$254 \quad LL(\theta = \{K_0, \alpha\}; X) = \ln(K_0) \sum_{i=1}^N n_i + \alpha \sum_{i=1}^N [n_i (M_i - m_0)] - K_0 \sum_{i=1}^N \exp[\alpha (M_i - m_0)] - \sum_{i=1}^N \ln(n_i!) \quad (16)$$

256 (note that the last term can be set to 0 during  $LL$  maximization). For Southern  
 257 California, we obtain  $\alpha_{\text{MLE}} = 2.32$  (1.01 in  $\log_{10}$  scale) and  $K_0 = 0.025$  when  
 258 considering large  $M \geq 6$  mainshocks only to avoid the issues of scaling break and data  
 259 dispersion at lower magnitudes. This result, represented by the black solid line on  
 260 Figure 5b, is in agreement with previous studies in the same region (e.g., Helmstetter,  
 261 2003; Helmstetter et al., 2005; Zaliapin and Ben-Zion, 2013; Seif et al., 2017) and  
 262 with  $\alpha = \ln(10) \approx 2.30$  predicted for large mainshocks in Solid Seismicity (Eq. 12).  
 263 Moreover we find a bulk  $\beta_{\text{MLE}} = 2.34$  (1.02 in  $\log_{10}$  scale) (Aki, 1965), in agreement  
 264 with  $\alpha \equiv \beta$ .

265 Let us now rewrite the Solid Seismicity aftershock productivity law (Eq. 12)  
 266 by only considering the large  $M$  case and injecting  $r_* = Fw_0$  (by combining Eqs. 7-8).  
 267 We get

$$268 \quad K(M > M_{\text{break}}) = \delta_+ \{2r_* \exp[\ln(10)(M - 4)] + \pi r_*^2 w_0\} \quad (17)$$

269 The role of  $w_0$  is illustrated in Figure 5b for different values (dashed and dotted  
 270 curves) and shown to be insignificant for large  $M$  values. Therefore Eq. (17) can be  
 271 approximated to

272  $K(M > M_{break}) \approx 2\delta_+ r_* \exp[\ln(10)(M - 4)]$  (18)

273 By analogy with Eq. (1), we get

274  $\delta_+ = \frac{K_0 \exp[\ln(10)(4 - m_0)]}{2r_*}$  (19)

275 With  $r_* \approx 1$  km estimated from  $\rho(r)$  (section 3.2) and  $K_0 = 0.025$ , we obtain  $\delta_+ = 1.23$   
 276 events/km<sup>3</sup> for  $m_0 = 2$ . We then get back the plateau  $\rho(r < r_*)$  for different  $M$  values  
 277 from Eq. (14), as shown in Figure 5a (horizontal dashed colored lines). Although  
 278 based on limited data, this result suggests that the activation parameter  $\delta_+$  is constant  
 279 (at least for large  $M$ ) in Southern California. Note that if  $\rho(r < r_*)$  was well  
 280 constrained, it could have been estimated jointly with  $r_*$  from Figure 5a to predict the  
 281 aftershock productivity law of Figure 5b without further fitting required (hence  
 282 removing  $K_0$  from the equation,  $K_0$  having no physical meaning in Solid Seismicity).

283

#### 284 **4. Role of aftershock selection on productivity scaling-break**

285 We tested the following piecewise model to identify any break in scaling at  
 286 smaller  $M$ , as predicted by Eq. (12):

287 
$$K(M) = \begin{cases} K_0 \frac{\exp[\ln(10)(M_{break} - m_0)]}{\exp[\frac{3}{2}\ln(10)(M_{break} - m_0)]} \exp\left[\frac{3}{2}\ln(10)(M - m_0)\right] & , M \leq M_{break} \\ K_0 \exp[\ln(10)(M - m_0)] & , M > M_{break} \end{cases}$$

288 (20)

289 but with the best MLE result obtained for  $M_{break} = m_0$ , suggesting no break in scaling  
 290 in the aftershock productivity data, as observed in Figure 6a. Final parameter  
 291 estimates are  $\alpha_{MLE} = 1.95$  (0.85 in log<sub>10</sub> scale) and  $K_0 = 0.141$  for the full mainshock  
 292 magnitude range  $M \geq m_0$  (dotted line), subject to high scattering at low  $M$  values.

293 We now identify whether the lack of break in scaling in aftershock  
 294 productivity observed in earthquake catalogues could be an artefact related to the

295 aftershock selection method. We run Epidemic-Type Aftershock Sequence (ETAS)  
 296 simulations (Ogata, 1988; Ogata and Zhuang, 2006), with the seismicity rate

$$297 \quad \begin{cases} \lambda(t, x, y) = \mu(t, x, y) + \sum_{i: t_j < t} K(M_i) f(t - t_i) g(x - x_i, y - y_i | M_i) \\ f(t) = c^{p-1} (p - 1) (t + c)^{-p} \\ g(x, y | M) = \frac{1}{\pi} (d e^{\gamma(M - m_0)})^{q-1} (x^2 + y^2 + d e^{\gamma(M - m_0)})^{-q} (q - 1) \end{cases} \quad (21)$$

298 Aftershock sequences are defined by power laws, both in time and space (for an  
 299 alternative temporal function, see Mignan (2015; 2016b); the spatial power-law  
 300 distribution is in agreement with Solid Seismicity in the case of a heterogeneous static  
 301 stress field – see section 2.2).  $\mu$  is the Southern California background seismicity, as  
 302 defined by the nearest-neighbor method (with same  $t, x, y$  and  $m$ ). We fix the ETAS  
 303 parameters to  $\theta = \{c = 0.011 \text{ day}, p = 1.08, d = 0.0019 \text{ km}^2, q = 1.47, \gamma = 2.01, \beta =$   
 304  $2.29, K_0 = 0.08\}$ , following the fitting results of Seif et al. (2017) for the Southern  
 305 California relocated catalog and  $m_0 = 2$  (see their Table 1). However, we define the  
 306 productivity function  $K(M)$  from Eq. (20) with  $M_{break} = 5$ . Examples of ETAS  
 307 simulations are shown in Figure 6b for comparison with the observed Southern  
 308 California time series. Figure 6c allows us to verify that the simulated aftershock  
 309 productivity is kinked at  $M_{break}$ , as defined by Eq. (20).

310 We then select aftershocks from the ETAS simulations with the nearest-  
 311 neighbor method. Figure 4d represents the estimated aftershock productivity, which  
 312 has lost the break in scaling originally implemented in the simulations (with an  
 313 underestimated  $\alpha_{MLE} = 2.07$  as observed in the real case for  $M \geq m_0$ ). Note that a  
 314 similar result is obtained when using a windowing method (Gardner and Knopoff,  
 315 1974). This demonstrates that the theoretical break in scaling predicted in the  
 316 aftershock productivity law can be lost in observations due to an aftershock selection  
 317 bias, all declustering techniques assuming continuity over the entire magnitude range.  
 318 While such a bias is possible, it yet does not prove that the break in scaling exists. The

319 fact that a similar break in scaling was obtained in independent Coulomb stress  
320 simulations (Hainzl et al., 2010) however provides high confidence in our results.

321 One other possible explanation for lack of scaling break is that our  
322 demonstration assumes moment magnitudes while the Southern California catalogue  
323 is in local magnitudes. Deichmann (2017) demonstrated that while  $M_L \propto M_w$  at large  
324  $M$ ,  $M_L \propto 1.5M_w$  at smaller  $M$  values. This could in theory cancel the kink in real data.  
325 However the scaling break predicted by Deichmann (2017) occurs at several  
326 magnitude units below the geometric scaling break expected by Solid Seismicity,  
327 invalidating this second option for mid-range magnitudes  $M$ .

328

## 329 **5. Conclusions**

330 In the present study, a closed-form expression defined from geometric and  
331 static stress parameters was proposed (Eq. 12) to describe the empirical Utsu  
332 aftershock productivity law (Eq. 1). This demonstration is similar to the previous ones  
333 made by the author to explain precursory accelerating seismicity and induced  
334 seismicity (Mignan, 2012; 2016b). In all these demonstrations, the main physical  
335 parameters remain the same, i.e. the activation density  $\delta_+$  (also  $\delta_-$  and  $\delta_0$ ), the  
336 background stress amplitude range  $\Delta\sigma_*$ , and the solid envelope  $r_*$  which describes the  
337 geometry of the “seismicity solid” (Fig. 3a-b). Further studies will be needed to  
338 evaluate whether the  $\delta_+$  and  $\Delta\sigma_*$  parameters are universal or region-specific and if the  
339 same values apply to different types of seismicity at a same location.

340 Although the Solid Seismicity Postulate (SSP) (Eq. 5) remains to be proven, it  
341 is so far a rather convenient and pragmatic assumption to determine the physical  
342 parameters that play a first-order role in the behavior of seismicity. The similarity of  
343 the SSP-simulated and observed values of the power-law exponent  $q$  of the aftershock

344 spatial density distribution shows that the SSP is consistent with large aftershock  
345 observations once uniform noise is added to the stress field (Figs. 4d-5a). The impact  
346 of other types of noise on  $q$  has yet to be investigated. The SSP is also complementary  
347 to the more common simulations of static stress loading (King and Bowman, 2003)  
348 and static stress triggering (Hainzl et al., 2010).

349 Analytic geometry, providing both a visual representation and an analytical  
350 expression of the problem at hand (Fig. 3), represents a new approach to try to better  
351 understand the behavior of seismicity. Its current limitation in the case of aftershock  
352 analysis consists in assuming that the static stress field is radial and described by Eq.  
353 (6) (e.g., Dieterich, 1994), which is likely only valid for mainshocks relieving most of  
354 the regional stresses and with aftershocks occurring on optimally oriented faults (King  
355 et al., 1994). More complex, second-order, stress behaviors might explain part of the  
356 scattering observed around Eq. (1) (Fig. 6a), such as overpressure due to trapped high-  
357 pressure gas for example (Miller et al., 2004 – see also Mignan (2016a) for an  
358 overpressure field due to fluid injection). Other  $\sigma(r)$  formulations could be tested in  
359 the future, the only constraint on generating so-called seismicity solids being the use  
360 of the postulated static stress step function of Eq. (5) (i.e., the Solid Seismicity  
361 Postulate, SSP).

362 Finally, the disappearance of the predicted scaling break in the aftershock  
363 productivity law once declustering is applied (Fig. 6) indicates that more work is  
364 required in that domain. Only a declustering technique that does not dictate a constant  
365 scaling at all  $M$  will be able to identify rather a scaling break really exists or not.

366

367 *Acknowledgments:* I thank N. Wetzler and two anonymous reviewers, as well as  
368 editor Ilya Zaliapin, for their valuable comments.



369

370 **References**

- 371 Abercrombie, R. and Leary, P.: Source parameters of small earthquakes recorded at  
372 2.5 km depth, Cajon Pass, Southern California: Implications for earthquake  
373 scaling, *Geophys. Res. Lett.*, 20, 1511-1514, 1993.
- 374 Aki, K.: Maximum Likelihood Estimate of  $b$  in the Formula  $\log N = a - bM$  and its  
375 Confidence Limits, *Bull. Earthq. Res. Instit.*, 43, 237-239, 1965.
- 376 Båth, M.: Lateral inhomogeneities of the upper mantle, *Tectonophysics*, 2, 483-514,  
377 1965.
- 378 Clauset, A., Shalizi, C. R. and Newman, M. E. J.: Power-Law Distributions in  
379 Empirical Data, *SIAM Review*, 51, 661-703, doi: 10.1137/070710111, 2009.
- 380 Deichmann, N.: Theoretical Basis for the Observed Break in  $M_L/M_w$  Scaling between  
381 Small and Large Earthquakes, *Bull. Seismol. Soc. Am.*, 107, doi:  
382 10.1785/0120160318, 2017.
- 383 Dieterich, J.: A constitutive law for rate of earthquake production and its application  
384 to earthquake clustering, *J. Geophys. Res.*, 99, 2601-2618, 1994.
- 385 Fan, W. and Shearer, P. M.: Local near instantaneously dynamically triggered  
386 aftershocks of large earthquakes, *Science*, 353, 1133-1136, 2016.
- 387 Felzer, K. R. and Brodsky, E. E.: Decay of aftershock density with distance indicates  
388 triggering by dynamic stress, *Nature*, 441, 735-738, doi: 10.1038/nature04799,  
389 2006.
- 390 Gardner, J. K. and Knopoff, L.: Is the sequence of earthquakes in Southern California,  
391 with aftershocks removed, Poissonian?, *Bull. Seismol. Soc. Am.*, 64, 1363-1367,  
392 1974.

393 Gu, C., Schumann, A. Y., Baisesi, M. and Davidsen, J.: Triggering cascades and  
394 statistical properties of aftershocks, *J. Geophys. Res. Solid Earth*, 118, 4278-4295,  
395 doi: 10.1002/jgrb.50306, 2013.

396 Gutenberg, B. and Richter, C. F.: Frequency of earthquakes in California, *Bull.*  
397 *Seismol. Soc. Am.*, 34, 185-188, 1944.

398 Hainzl, S., Brietzke, G. B. and Zöller, G.: Quantitative earthquake forecasts resulting  
399 from static stress triggering, *J. Geophys. Res.*, 115, B11311, doi:  
400 10.1029/2010JB007473, 2010.

401 Hauksson, E., Yang, W. and Shearer, P. M.: Waveform Relocated Earthquake Catalog  
402 for Southern California (1981 to June 2011), *Bull. Seismol. Soc. Am.*, 102, 2239-  
403 2244, doi: 10.1785/0120120010, 2012.

404 Helmstetter, A.: Is Earthquake Triggering Driven by Small Earthquakes?, *Phys. Rev.*  
405 *Lett.*, 91, doi: 10.1102/PhysRevLett.91.058501, 2003.

406 Helmstetter, A., Kagan, Y. Y. and Jackson, D. D. : Importance of small earthquakes  
407 for stress transfers and earthquake triggering, *J. Geophys. Res.*, 110, B05S08, doi:  
408 10.1029/2004JB003286, 2005.

409 Kanamori, H. and Anderson, D. L.: Theoretical basis of some empirical relations in  
410 seismology, *Bull. Seismol. Soc. Am.*, 65, 1073-1095, 1975.

411 King, G. C. P., Stein, R. S. and Lin, J.: Static Stress Changes and the Triggering of  
412 Earthquakes, *Bull. Seismol. Soc. Am.*, 84, 935-953, 1994.

413 King, G. C. P. and Bowman, D. D.: The evolution of regional seismicity between  
414 large earthquakes, *J. Geophys. Res.*, 108, 2096, doi: 10.1029/2001JB000783, 2003.

415 Lin, J. and Stein, R. S.: Stress triggering in thrust and subduction earthquakes, and  
416 stress interaction between the southern San Andreas and nearby thrust and strike-  
417 slip faults, *J. Geophys. Res.*, 109, B02303, doi: 10.1029/2003JB002607, 2004.

418 Lippiello, E., de Arcangelis, J. and Godano, C.: Role of Static Stress Diffusion in the  
419 Spatiotemporal Organization of Aftershocks, *Phys. Rev. Lett.*, 103, 038501, doi:  
420 10.1103/PhysRevLett.103.038501, 2009.

421 Marsan, D. and Lengliné, O.: A new estimation of the decay of aftershock density  
422 with distance to the mainshock, *J. Geophys. Res.*, 115, B09302, doi:  
423 10.1029/2009JB007119, 2010.

424 Miller, S. A., Collettini, C., Chiaraluce, L., Cocco, M., Barchi, M. and Kaus, B. J. P.:  
425 Aftershocks driven by a high-pressure CO<sub>2</sub> source at depth, *Nature*, 427, 724-727

426 Mignan, A., King, G. C. P. and Bowman, D.: A mathematical formulation of  
427 accelerating moment release based on the stress accumulation model, *J. Geophys.*  
428 *Res.*, 112, B07308, doi: 10.1029/2006JB004671, 2007.

429 Mignan, A.: Non-Critical Precursory Accelerating Seismicity Theory (NC PAST) and  
430 limits of the power-law fit methodology, *Tectonophysics*, 452, 42-50, doi:  
431 10.1016/j.tecto.2008.02.010, 2008.

432 Mignan, A.: Retrospective on the Accelerating Seismic Release (ASR) hypothesis:  
433 Controversy and new horizons, *Tectonophysics*, 505, 1-16, doi:  
434 10.1016/j.tecto.2011.03.010, 2011.

435 Mignan, A.: Seismicity precursors to large earthquakes unified in a stress  
436 accumulation framework, *Geophys. Res. Lett.*, 39, L21308, doi:  
437 10.1029/2012GL053946, 2012.

438 Mignan, A.: Modeling aftershocks as a stretched exponential relaxation, *Geophys.*  
439 *Res. Lett.*, 42, 9726-9732, doi: 10.1002/2015GL066232, 2015.

440 Mignan, A.: Static behaviour of induced seismicity, *Nonlin. Processes Geophys.*, 23,  
441 107-113, doi: 10.5194/npg-23-107-2016, 2016a.

442 Mignan, A.: Reply to “Comment on ‘Revisiting the 1894 Omori Aftershock Dataset  
443 with the Stretched Exponential Function’ by A. Mignan” by S. Hainzl and A.  
444 Christophersen, *Seismol. Res. Lett.*, 87, 1134-1137, doi: 10.1785/0220160110,  
445 2016b.

446 Moradpour, J., Hainzl, S. and Davidsen, J.: Nontrivial decay of aftershock density  
447 with distance in Souther California, *J. Geophys. Res. Solid Earth*, 119, 5518-5535,  
448 doi: 10.1002/2014JB010940, 2014.

449 Ogata, Y.: Statistical Models for Earthquake Occurrences and Residual Analysis for  
450 Point Processes, *J. Am. Stat. Assoc.*, 83, 9-27, 1988.

451 Ogata, Y. and Zhuang, J.: Space-time ETAS models and an improved extension,  
452 *Tectonophysics*, 413, 13-23, doi: 10.1016/j.tecto.2005.10.016, 2006.

453 Richards-Dinger, K., Stein, R. S. and Toda, S.: Decay of aftershock density with  
454 distance does not indicate triggering by dynamic stress, *Nature*, 467, 583-586, doi:  
455 10.1038/nature09402, 2010.

456 Ross, Z. E., Hauksson, E. and Ben-Zion, Y.: Abundant off-fault seismicity and  
457 orthogonal structures in the San Jacinto fault zone, *Sci. Adv.*, 3, doi:  
458 10.1126/sciadv.1601946, 2017.

459 Seif, S., Mignan, A., Zechar, J. D., Werner, M. J. and Wiemer, S.: Estimating ETAS:  
460 The effects of truncation, missing data, and model assumptions, *J. Geophys. Res.*  
461 *Solid Earth*, 121, 449-469, doi: 10.1002/2016JB012809, 2017.

462 Shapiro, S. A. and Dinske, C.: Scaling of seismicity induced by nonlinear fluid-rock  
463 interaction, *J. Geophys. Res.*, 114, B09307, doi: 10.1029/2008JB006145, 2009.

464 Shaw, B. E. and Scholz, C. H.: Slip-length scaling in large earthquakes: Observations  
465 and theory and implications for earthquake physics, *Geophys. Res. Lett.*, 28, 2995-  
466 2998, 2001.

467 Shearer, P. M.: Space-time clustering of seismicity in California and the distance  
468 dependence of earthquake triggering, *J. Geophys. Res.*, 117, B10306, doi:  
469 10.1029/2012JB009471, 2012.

470 Toda, S., Stein, R. S., Richards-Dinger, K. and Bozkurt, S.: Forecasting the evolution  
471 of seismicity in southern California: Animations built on earthquake stress transfer,  
472 *J. Geophys. Res.*, 110, B05S16, doi: 10.1029/2004JB003415, 2005.

473 Tormann, T., Wiemer, S. and Mignan, A.: Systematic survey of high-resolution b  
474 value imaging along Californian faults: inference on asperities, *J. Geophys. Res.*  
475 *Solid Earth*, 119, 2029-2054, doi: 10.1002/2013JB010867, 2014.

476 Utsu, T.: Aftershocks and Earthquake Statistics (1): Some Parameters Which  
477 Characterize an Aftershock Sequence and Their Interrelations, *J. Faculty Sci.*  
478 *Hokkaido Univ. Series 7 Geophysics*, 3, 129-195, 1970a.

479 Utsu, T.: Aftershocks and Earthquake Statistics (2): Further Investigation of  
480 Aftershocks and Other Earthquake Sequences Based on a New Classification of  
481 Earthquake Sequences, *J. Faculty Sci. Hokkaido Univ. Series 7 Geophysics*, 3,  
482 197-266, 1970b.

483 Utsu, T., Ogata, Y. and Matsu'ura, R. S.: The Centenary of the Omori Formula for a  
484 Decay Law of Aftershock Activity, *J. Phys. Earth*, 43, 1-33, 1995.

485 van der Elst, N. J. and Shaw, B. E.: Larger aftershocks happen farther away:  
486 Nonseparability of magnitude and spatial distributions of aftershocks, *Geophys.*  
487 *Res. Lett.*, 42, 5771-5778, doi: 10.1002/2015GL064734, 2015.

488 Varnes, D. J.: Predicting Earthquakes by Analyzing Accelerating Precursory Seismic  
489 Activity, *Pure Appl. Geophys.*, 130, 661-686, 1989.

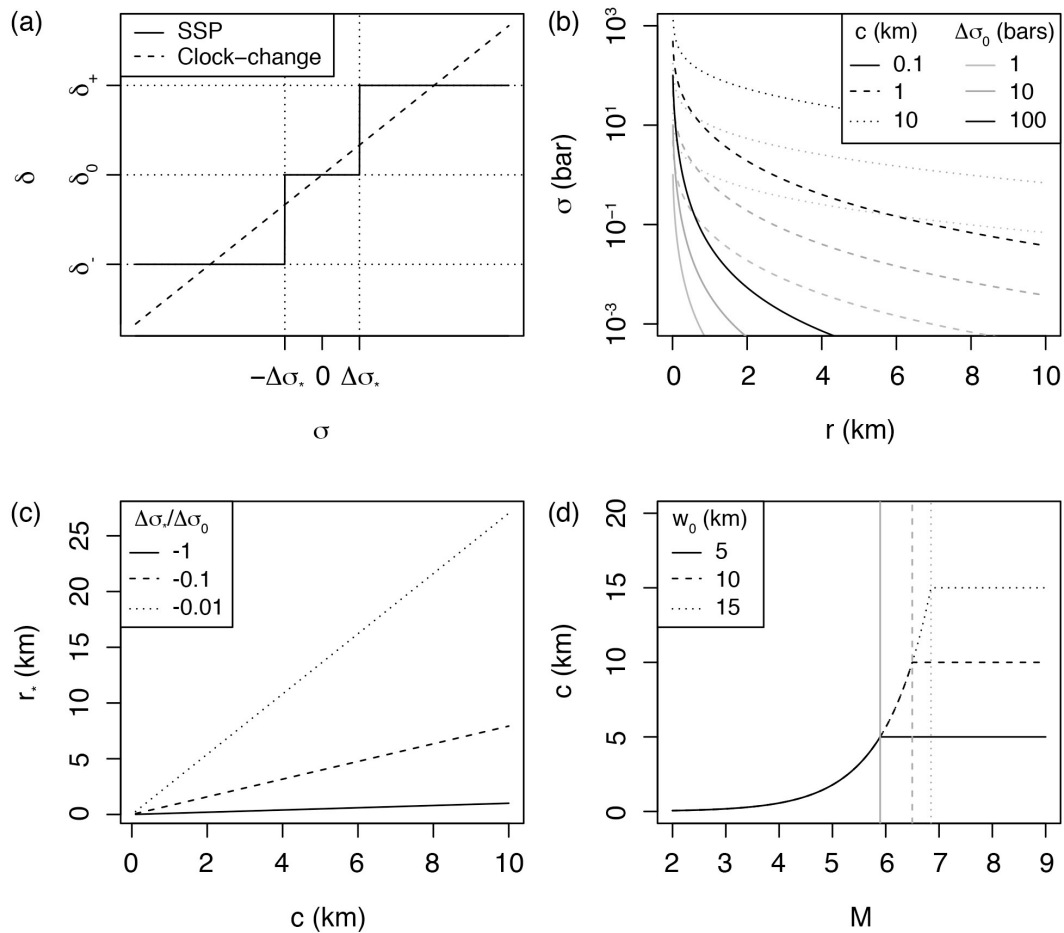
490 Yamanaka, Y. and Shimazaki, K.: Scaling Relationship between the Number of  
491 Aftershocks and the Size of the Main Shock, *J. Phys. Earth*, 38, 305-324, 1990.

492 Zaliapin, I., Gabrielov, A., Keilis-Borok, V. and Wong, H.: Clustering Analysis of  
 493 Seismicity and Aftershock Identification, Phys. Rev. Lett., 101, 018501, doi:  
 494 10.1103/PhysRevLett.101.018501, 2008.

495 Zaliapin, I. and Ben-Zion, Y.: Earthquake clusters in southern California I:  
 496 Identification and stability, J. Geophys. Res. Solid Earth, 118, 2847-2864, doi:  
 497 10.1002/jgrb.50179, 2013.

498

499 **Figures**



500

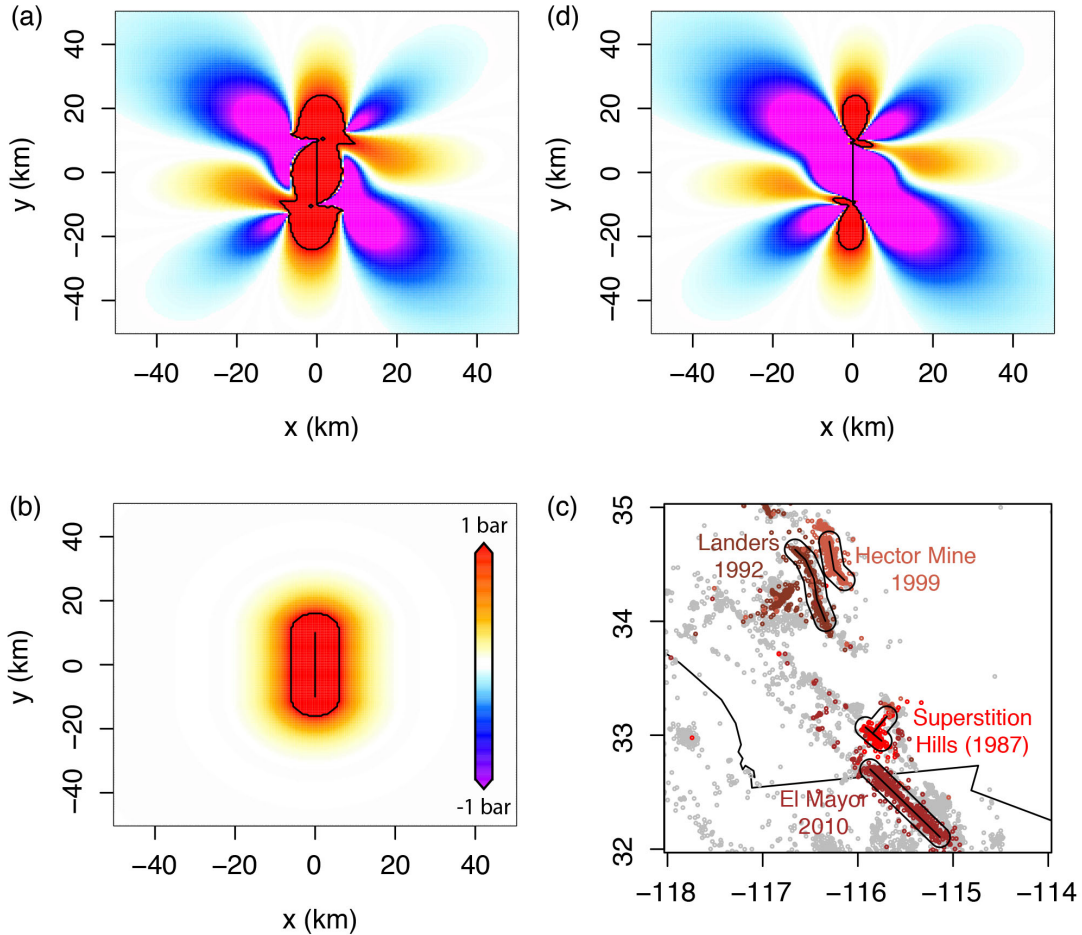
501 **Figure 1.** Definition of the aftershock solid envelope in a permanent static stress field:

502 (a) Event density stress step-function  $\delta(\sigma)$  (Eq. 5) of the Solid Seismicity Postulate

503 (SSP) in comparison to the linear clock-change model; (b) Static stress  $\sigma$  versus

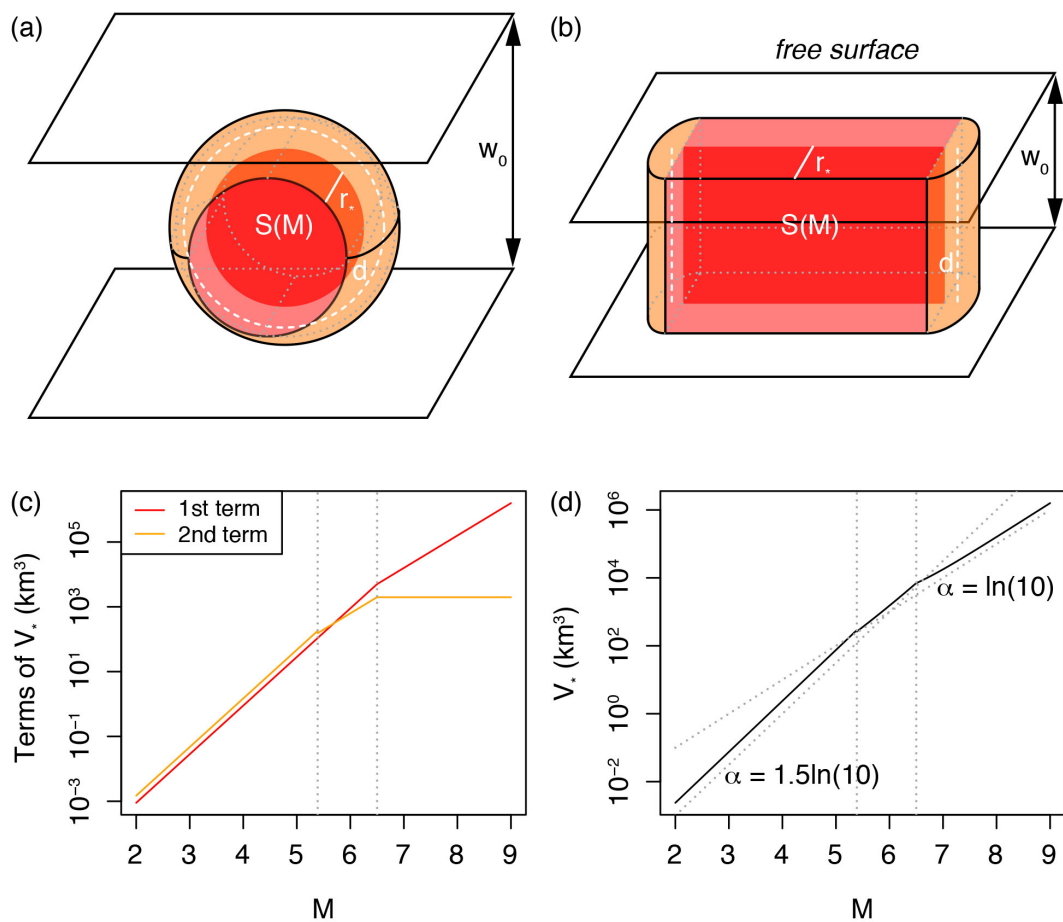
504 distance  $r$  for different effective crack radii  $c$  and rupture stress drops  $\Delta\sigma_0$  (Eq. 6); (c)

505 Linear relationship between effective crack radius  $c$  and aftershock solid envelope  
 506 radius  $r_*$  for different  $\Delta\sigma_*/\Delta\sigma_0$  ratios (Eq. 7); (d) Relationship between mainshock  
 507 magnitude  $M$  and effective crack radius  $c$  for different seismogenic widths  $w_0$  (Eq. 8).  
 508



509  
 510 **Figure 2.** Possible static stress fields and inferred aftershock spatial distribution: (a)  
 511 Right-lateral Coulomb stress field for optimally oriented faults, where the mainshock  
 512 relieves all of the regional stresses  $\sigma_r = 10$  bar, with  $\Delta\sigma_0 \approx -Gs/L \approx -10$  bar ( $G =$   
 513  $3.3 \cdot 10^5$  bar the shear modulus,  $s = 0.6$  m the slip,  $L = 20$  km the fault length, and  $w =$   
 514  $10$  km the fault width); (b) Radial static stress field computed from Eq. (6) with  $\Delta\sigma_0 =$   
 515  $-10$  bar and  $c = \sqrt{(Lw)/\pi}$  for consistency with (a); (c) Aftershock distribution of the  
 516 largest strike-slip events in the Southern California relocated catalog, identified here

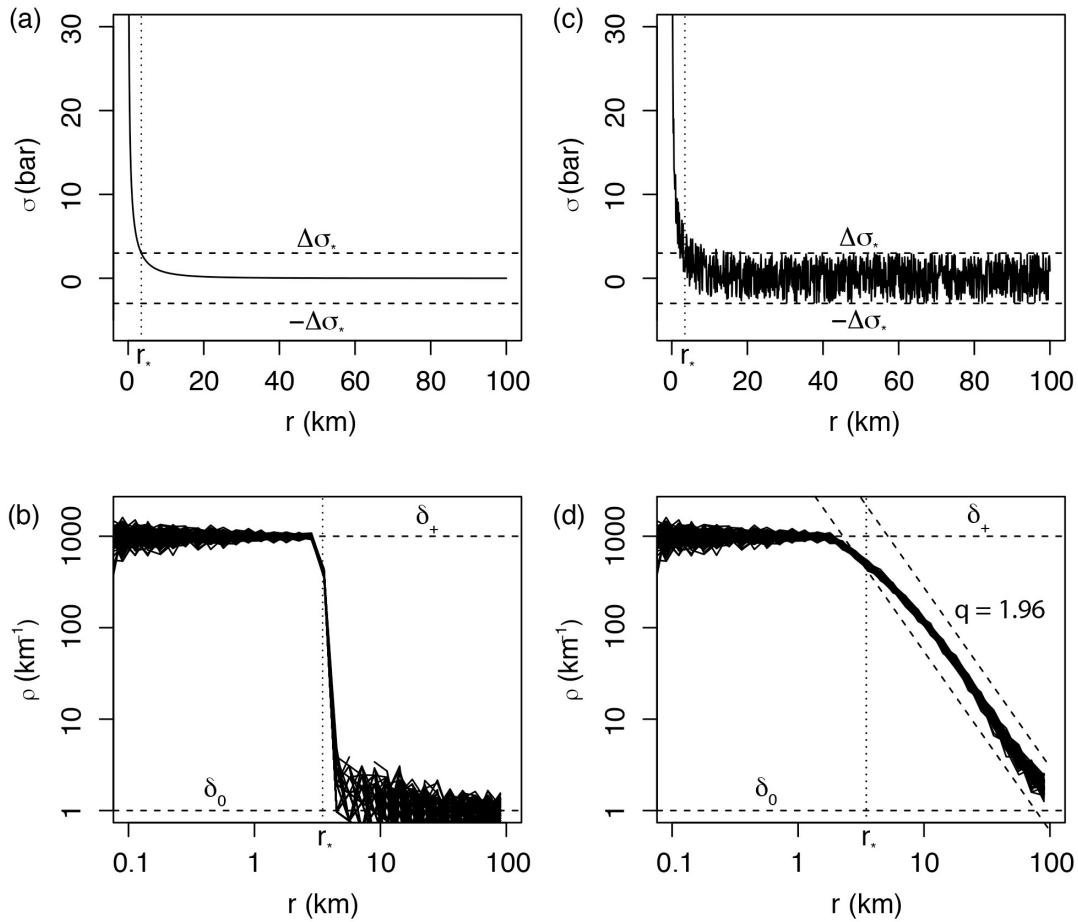
517 as all events occurring within one day of the mainshock (see Data section 3.1); (d)  
 518 Right-lateral Coulomb stress field for optimally oriented faults, where the mainshock  
 519 relieves only a fraction of the regional stresses  $\sigma_r = 100$  bar with  $\Delta\sigma_0 = -10$  bar (same  
 520 rupture as in (a)) – The black contour represents 1 bar in (a), (b) and (d), and a 10 km  
 521 distance from rupture in (c). Coulomb stress fields of (a) and (d) were computed using  
 522 the Coulomb 3 software (Lin and Stein, 2004; Toda et al., 2005).  
 523



524  
 525 **Figure 3.** Geometric origin of the aftershock productivity law: (a) Sketch of the  
 526 aftershock solid for a small mainshock rupture represented by a disk; (b) Sketch of the  
 527 aftershock solid for a large mainshock rupture represented by a rectangle; (c) Relative  
 528 role of the two terms of Eq. (9), here with  $w_0 = 10$  km and  $\frac{\Delta\sigma_*}{\Delta\sigma_0} = -0.1$  (to first estimate  
 529  $c$  and  $r_*$  from Eqs. 8 and 7, respectively); (d) Aftershock productivity law (normalized

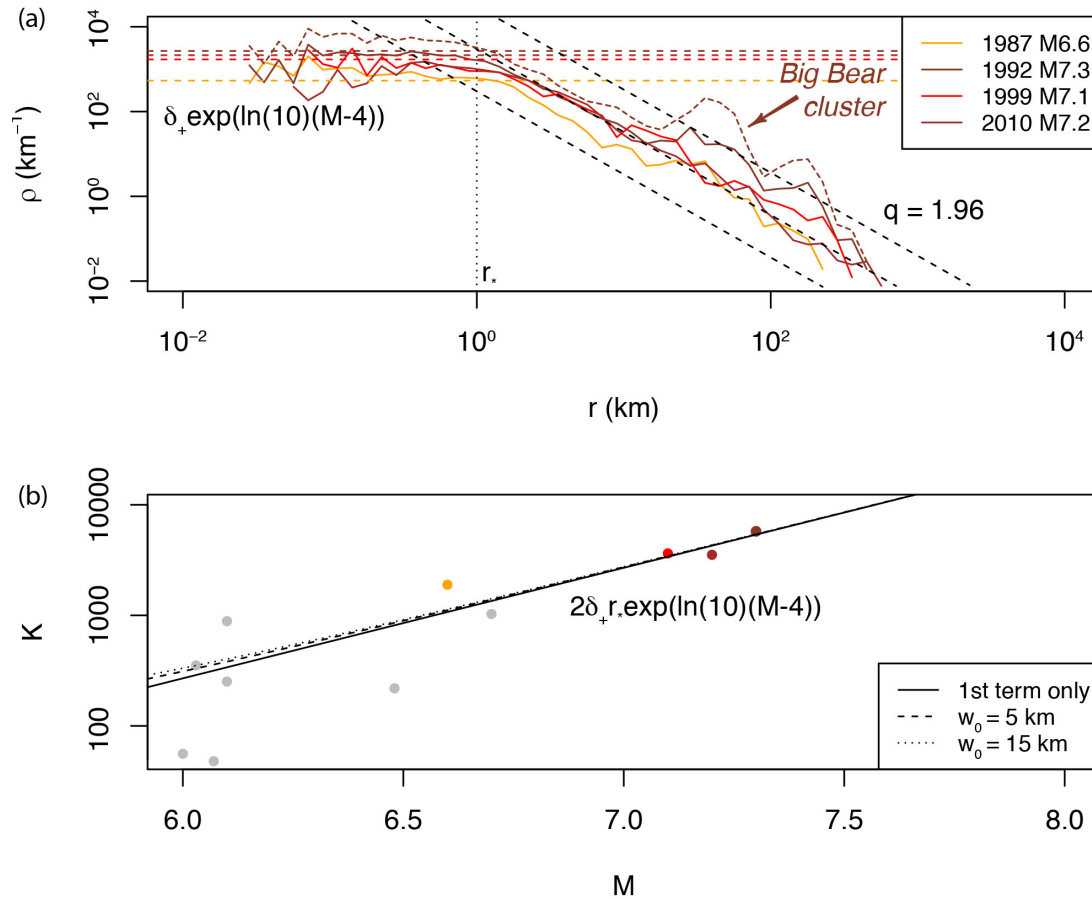


530 by  $\delta_+$ ) predicted by Solid Seismicity (Eq. 11). This relationship is of the same form as  
 531 the Utsu productivity law (Eq. 1) for large  $M$  (see text for an explanation of the lack  
 532 of break in scaling in Eq. 1 for small  $M$ ). Dotted vertical lines represent  $M$  for  
 533  $c(M) + r_*(M) = \frac{w_0}{2}$  and  $S(M) = \pi w_0^2$ , respectively.  
 534



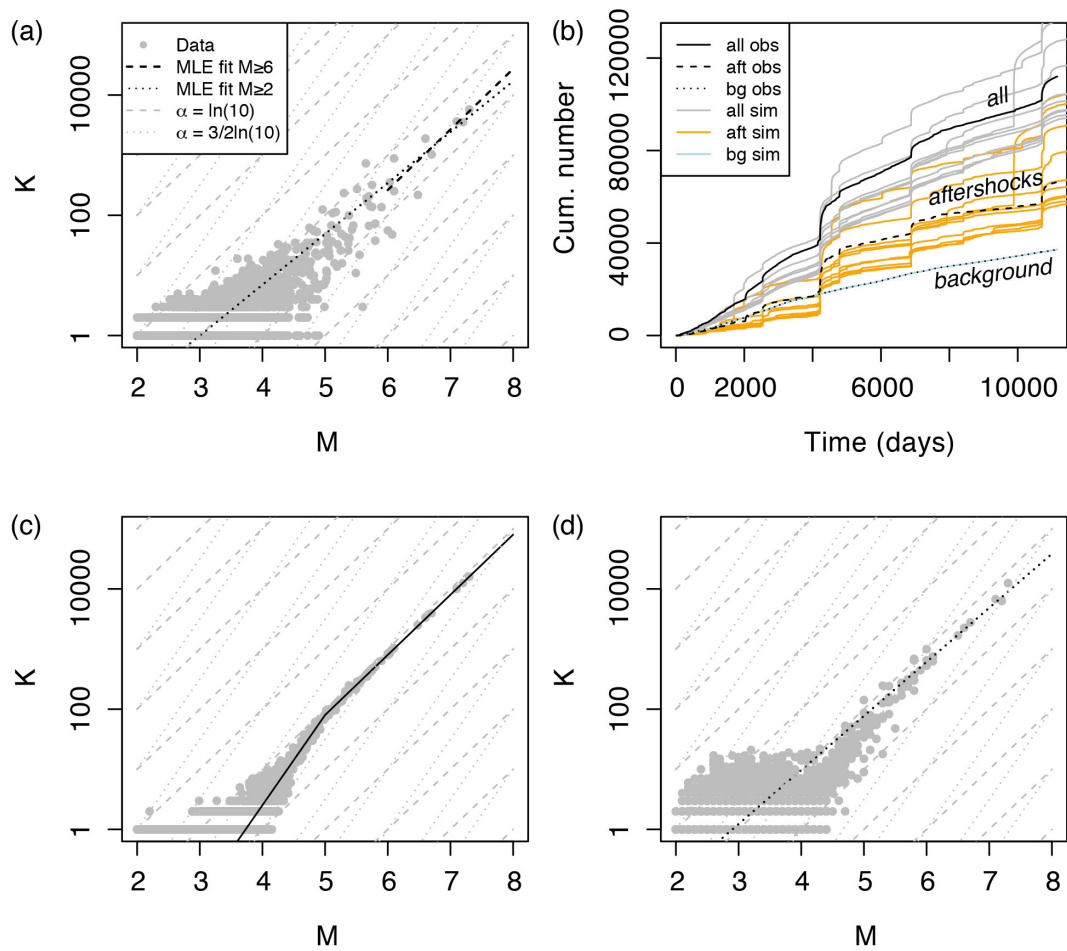
535  
 536 **Figure 4.** Spatial distribution of aftershocks following the SSP. (a) Smooth static  
 537 stress field as a function of distance  $r$  from the mainshock, with  $\Delta\sigma_0 = -10$  bar and  $c =$   
 538 10 km (Eq. 6); (b) Step-like aftershock spatial linear density  $\rho(r)$  with  $\delta_+ = 1000$   
 539 events per km,  $\delta_0 = 1$  event per km and  $\Delta\sigma_* = -0.3\Delta\sigma_0$  (*ad-hoc* ratio yielding  $r_* = 3.5$   
 540 km; Eq. (7) – event distances sampled from the  $\delta(r)$  distribution, repeated 100 times).  
 541 Such distribution is not observed in Nature; (c) Same as (a) but with random uniform

542 noise representative of spatial heterogeneities added to the regional stress field; (d)  
 543 Power-law-like aftershock spatial linear density  $\rho(r)$  with power exponent MLE  
 544 estimate  $q = 1.96$ , representative of real aftershock observations (see Fig. 5a), due to  
 545 the addition of uniform noise to the static stress field.  
 546



547  
 548 **Figure 5.** Estimating the Solid Seismicity parameters from the spatial distribution of  
 549 aftershocks: (a) Spatial linear density distribution  $\rho(r)$  of aftershocks for the four  
 550 largest strike-slip mainshocks in Southern California (with first-generation  
 551 aftershocks only; the density distribution comprising all aftershocks generated by the  
 552 Landers mainshock is represented by the dotted curve to illustrate the type of spatial  
 553 heterogeneity, such as the Big Bear cluster, not considered in the present study – see  
 554 also Fig. 2c). The Solid Seismicity parameters  $r_* = 1$  km and  $\delta_+(m_0 = 2) = 1.23$

555 events/km<sup>3</sup> can be retrieved from the observed plateau  $\rho(r < r_*)$ , in agreement with the  
 556 SSP (see Fig. 4d). Note that the spatial power-law decay at high  $r$  is similar to the one  
 557 expected by the SSP in the case of a static stress field with additive uniform noise  
 558 (expected  $q = 1.96$  represented by the dashed black lines); (b) Aftershock productivity  
 559  $K$  for  $M > 6$ . The curves represent the productivity law as defined by Solid Seismicity  
 560 (Eq. 17) for different  $w_0$  values (first term only corresponds to  $w_0 = 0$ ; Eq. 18).  
 561



562  
 563 **Figure 6.** Aftershock productivity defined as the number of aftershocks  $K(m_0 = 2)$  per  
 564 mainshock of magnitude  $M$ : (a) Observed aftershock productivity in Southern  
 565 California with aftershocks selected using the nearest-neighbor method; (b)  
 566 Seismicity time series with distinction made between background events and

567 aftershocks, observed (“obs”, in black) and ETAS-simulated (“sim”, colored); (c)  
568 True simulated aftershock productivity with kink, defined from Eq. (20); (d)  
569 Retrieved simulated aftershock productivity with aftershocks selected using the  
570 nearest-neighbor method - Data points in (a), (c) and (d) are represented by grey dots;  
571 the model MLE fits are represented by the dashed and dotted black lines for  $M \geq 6$   
572 and  $M \geq m_0$ , respectively; dashed and dotted grey lines are visual guides to  $\alpha =$   
573  $3/2\ln(10)$  and  $\ln(10)$ , respectively.  
574